Alexandria Engineering Journal (2023) 66, 1–14

HOSTED BY

ELSEVIER

Alexandria University

Alexandria Engineering Journal

www.elsevier.com/locate/aej
www.sciencedirect.com

ORIGINAL ARTICLE

Experimental investigations on cryogenic friction-stir welding of similar ZE42 magnesium alloys

Pavel Trojovský [a], Vigneswaran Dhasarathan [b], Sampath Boopathi [c,*]

[a] Department of Mathematics, Faculty of Science, University of Hradec Králové, 50003, Czech Republic
[b] Department of Applied Physics, University of Hradec Králové, 50003, Czech Republic
[c] Department of Mechanical Engineering, Muthayammal Engineering College, Rasipuram, Tamil Nadu, 637 408, India

Received 5 September 2022; revised 7 November 2022; accepted 4 December 2022
Available online 14 December 2022

KEYWORDS

Liquid Nitrogen;
Microstructure;
Tensile Strength;
Hardness;
Wear Rate;
Taguchi Technique;
Comparisons

Abstract In this research, the cryogenic friction stir welding (CFSW) process has been performed using a liquid nitrogen medium to join two similar ZE42 magnesium alloy plates. The new experimental setup has been designed and fabricated to supply low-temperature (−196 °C) liquid nitrogen into the welding zone. The effects of welding parameters (tool pin profile, tool rotational speed, welding speed, and axial load) on the welding characteristics (tensile strength, hardness, and wear rate) have been investigated by the Taguchi technique. The impacts of welding parameters have been analysed to predict the optimum welding characteristics. The predicted best welding settings have been utilized to compare the CFSW and normal friction stir welding (NFSW) performances. The fractography of tensile-tested specimens, hardness distributions, and microstructure of worn-out CFSW welding surfaces have been examined by scanning electron microscopy (SEM) analysis. When compared to the NFSW process, the tensile strength and hardness of CFSW are improved by 41.36 % and 35.13 %, respectively, and the wear rate has decreased by 23.53 %.

1. Introduction

The light weighted magnesium and its alloys are widely used in automotive and aerospace industrial applications to reduce vehicle weight, fuel consumption, and emission rates [1,2]. The weight of the magnesium alloy is shown to be between 35 and 78 percent lighter than that of the alloys of aluminium and steel [3]. However, its strength and ductility are limited due to poor formability and stability above room temperature during the conventional fusion welding process [4]. The FSW is a solid-state joining technique involving the application of heat and frictional energies for attaining quality and defect-free welds. However, the defect-free FSW of magnesium alloys is now facing a lot of technical deficiencies. Porosity, cracks, segregation, brittle intermetallic formation, oxide film formation, and liquation cracking problems have been observed during the FSW of Mg alloys [5]. Many research attempts have been made to eliminate the above-mentioned FSW issues. However, the defect-free FSW of magnesium alloy joints should be

* Corresponding author.
E-mail addresses: pavel.trojovsky@uhk.cz (P. Trojovský), dhasavi1@uhk.cz (V. Dhasarathan), boopathis@bitsathy.ac.in, boopasangee@gmail.com (S. Boopathi).

Peer review under responsibility of Faculty of Engineering, Alexandria University.

https://doi.org/10.1016/j.aej.2022.12.007
1110-0168

attained to meet the requirements of industry. The ZE42 alloy is a nickel–iron-magnesium superalloy that is used in furnaces, nuclear power plants to observe neutrons, automobiles, aerospace, and transport applications due to its excellent mechanical properties [6]. However, the FSW of ZE42 alloys is welded with many defects when using atmospheric and air environment conditions. While using the liquid medium in the FSW process, the heat-carrying capacity of water or liquid is higher than atmospheric air conditions. The microstructure in the FSW zone has rapidly been modified, and tensile strength is also improved by coolant [7]. The following sections elaborate on the various impacts and improvements in FSW processes when using various welding mediums.

The heat-carrying capacity is improved by the water-assisted FSW of AZ91 magnesium alloys due to the minimization of grain size in the stir zone [8]. The grain size in various welding zones has been studied using submergible FSW of AZ61 alloy. The 2.8 μm grain size of particles in the welding zone was obtained by an underwater welding process due to grain refinement. In the air-based FSW process, 8.4 μm grain size of particles were found in the welding zone [9]. The underwater FSW process of Mg-Y-Nd alloy was investigated using a conical-shaped threaded tool. The average grain size was reported to be 1.5 μm due to rapid cooling by water [10]. When comparing base alloy materials, the micro-hardness FSW of soft alloy materials is reduced in liquid medium environments [11]. The use of a hot water environment increased the tensile strength and microhardness of the FSW weld [12]. The corrosion resistance, wear resistance, and negative corrosive potential of the submersible FSW process are preferred to those of the air FSW process [13,14]. The parametric analysis of the water-cooled, submerged FSW process was performed to investigate the effects of intermetallic components, high temperature, and hardness. The submersible welding process is well suited to reducing peak temperature and increasing micro-hardness [15]. Ultra-fine grains, nanograins, and nanograin boundaries were achieved during the cryogenic FSW process to improve mechanical and thermal stabilities, strength, and electric conductivity [16]. The cryogenic cooling process has primarily increased the percentages of elongation, toughness, impact, and fatigue strengths at the nugget zone [17]. The friction-stir-weldability relationship has been investigated in order to determine the relationship between mechanical and microstructural properties under cryogenic conditions. It was discovered that post-rolling of welded specimens improved welding strength, joint efficiency, and microstructure [18]. The dry ice-assisted FSW process also improved the microstructure, corrosion, and mechanical properties of the welded aluminium alloy[19,20]. The cryogenic FSW of similar magnesium alloys has been examined to improve the corrosion and wear resistance behaviours using liquid nitrogen coolant [3]. It was revealed from the welding of magnesium research articles that the welding defects had been obtained due to vaporising metal by the frictional heat[21].

Thus, the cryogenic friction stir welding method has been applied to improve the mechanical characteristics of friction stir welding of various alloys. It was also derived from the aforementioned research activities that there were no investigations found to weld the ZE42 alloy plates using cryogenic liquid nitrogen-assisted FSW. In this article, two ZE42 magnesium alloy plates are joined by the CFSW process to make the defect-free welding components. The experimental setup has been fabricated to supply liquid nitrogen into the welding zone. The Taguchi L27 orthogonal array has been used to design and conduct systematic experiments. It was predicted that the best combination of welding parameter settings would maximize the tensile strength, hardness, and wear rate. The welding performances of CFSW and NFSW processes are compared using the best predicted setting obtained by Taguchi analysis.

2. Materials and experimentation

2.1. Cryogenic friction stir welding (CFSW) setup

Generally, the NFSW process has been performed in atmospheric air environments. According to the literature, magnesium and its alloys are unstable during the NFSW process at maximum frictional temperatures[1,5]. A cryogenic investigation has been performed to overcome the above issue and improve the welding quality. In this research, the cryogenic cooled friction-stir-welding setup has been fabricated to perform defect-free welding process and enhance the welding quality in the non-flammable low-temperature (-196 °C) liquid nitrogen (LN2) medium. The various properties of LN2 are shown in Table 1. The schematic arrangement of the CFSW setup is illustrated in Fig. 1. The cryogenic tank has been connected to inlet and outlet tubes with no leaks.is connected to an air compressor, and the outlet is connected to the welding zone. While supplying pressurized air into the cryogenic container, the liquid nitrogen is accelerated, and pressurized liquid nitrogen is passed into the welding zone. When controlling the pressure of the air, the flow rate of the LN2 could be adjusted to the FSW zone. The LN2 hoses are placed at a 60-degree angle in the setup. To reduce excess heat development in the FSW zone, cryogenic liquid nitrogen is used. All the experiments have been conducted on a servo-controlled three-axis FSW machine. The butt joint arrangements in the welding table and CFSW experimental setup are shown in Fig. 2(a) and (b), respectively.

2.2. Material preparation

Two similar magnesium ZE42alloy (200 mm × 250 mm × 6 mm) plates have been joined using the cryogenic friction stir welding (CFSW) process. The chemical composition and mechanical properties of the ZE42 alloy are shown in Table 2. ZE42 alloy has been used in many automobile and aircraft component manufacturing applications due to its lightweight,

Table 1 Properties of cryogenic liquid nitrogen (LN_2) coolant.

Parameter	Properties	Unit
Flammable	Non-flammable Liquid Nitrogen	–
Boiling point	−195.687	°C
Freezing point	−209.8	°C
Triple point	−209.852	°C
Density of liquid	0.808	g/cm^3
Heat of vaporization		kJ/kg
Working Temperature	−196	°C

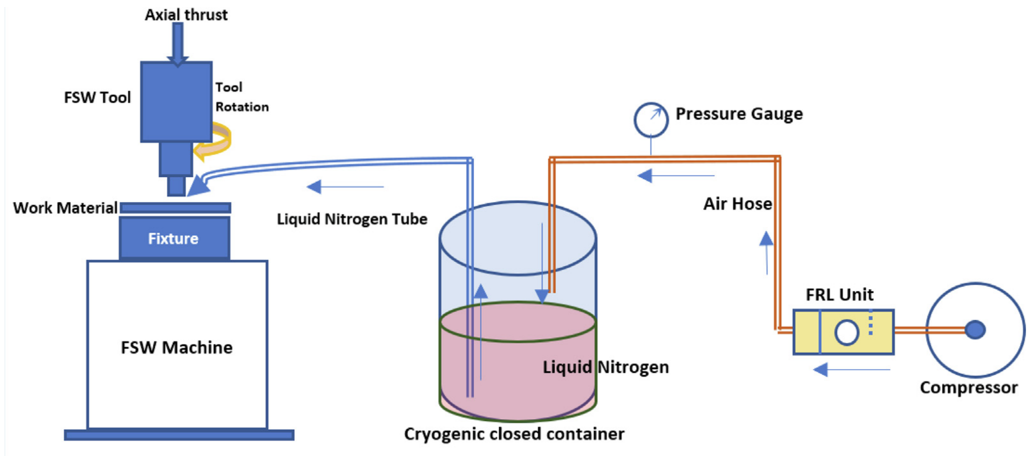

Fig. 1 Schematic arrangements of Cryogenic Friction Stir Welding Process.

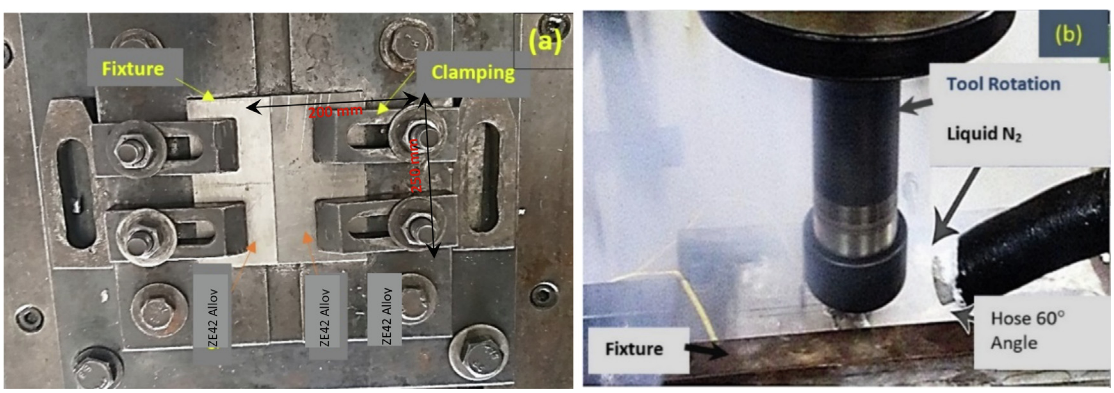

Fig. 2 FSW Experimental Setup (a) FSW Arrangements (b) Cryogenic FSW Process.

softness, ductility, good corrosion resistance, and weldability to make easy fabrication[22]. Three different profiles of H13 tool steel with 60 HRC are: cylinder, stepped cylinder, and stepped-square profiles. The pin-end diameter of cylindrical and stepped cylindrical tools is 5 mm [23]. The length of the stepped square at the pin end of the tool is 5 mm. The tool tilt angle is 20°.

2.3. Experimentations

All FSW experiments have been conducted under cryogenic conditions. Initially, the exploratory experiments were conducted based on the range of parameter settings in the FSW machine. These experiments were conducted using the "one variable at a time" approach[24,25]. During these tests, only one parameter is modified from a low level to a high level, and the remaining parameters are constantly maintained at their mean values. The ranges of parameters have been finalized and used for Taguchi's systematic experiments [26]. The values of the low, medium, and high levels of each parameter are displayed in Table 3. The Taguchi L27 orthogonal design was chosen based on three levels of four influencing parameters[27]. During the Taguchi design, interactions between the tool pin profile and rotational speed, welding speed, and axial load have been considered. However, the experiments have only been conducted using four parameters.

Table 2 Chemical elements and mechanical properties of ZE42 alloy.

Chemical Composition of the ZE42 Material (Weight %)					
Zinc	**Zirconium**	**Rhenium**	**Silicon**	**Manganese**	**Magnesium**
2.5 %	0.7 %	3.2 %	0.2 %	0.1 %	93.3 %
Mechanical Properties of the Base Materials ZE42 Alloy					
Melting Point	**Hardness**	**Ultimate tensile strength**	**Percentage of Elongation**		
548○C	65BHN	218 MPa	4.50 %		

The tool rotation speed and welding speed have been measured and adjusted by the control unit of the FSW machine. Tensile strength, hardness, and wear rate are considered response parameters. Because these welding characteristics play important roles in making automobile and aircraft components using ZE42, tensile strength is the key mechanical factor to withstand the load when welding supports[28]. The wear rate and hardness characteristics are also important for examining the frictional, inflationary, and corrosion resistances and oil resistances by steam, oil, and water of the welding joint[29].

After conducting the CFSW process, the specimen has been made as per the ASTM E-2448 standard for tensile and ASTM E10-18 standards for Brinell hardness tests using a wire-cut electric discharge machining process[3]. The schematic arrangement of the ASTM E-2448 specimen is shown in Fig. 3. The hardness tests were performed by a 10 mm steel ball indenter in the Brinell hardness testing instrument (ERNST-COMPUTEST-SC model). The tensile tests have been performed by a 50 KN capacity universal tensile testing machine[30]. The tensile strength has also been determined using tensile test observations. The wear rate on the stir-zone of the CFSW joint has been determined using a pin-on-disc instrument. The experiments were performed with a 1000 m sliding distance, 30 N of load, and 1500 rpm of rotation speed[31]. Equation (1) is used to calculate the wear rate as given below[31].

$$Wear\ rate = \frac{(Initial\ weight - Final\ weight\ after\ pin\ on\ disc\ test)}{Sliding\ distance \times Load \times Density}\ \mathrm{mm^3/Nm} \quad (1)$$

The experimental results of tensile strength, hardness, and wear rate are noted in Table 4. All the experiments were replicated two times to avoid experimental errors[32]. The mean and percentage of error between two replicated experimental values are shown in Table 5. The error values are less than 5 % of the confidence level [33,34]. In this research, the tensile strength and hardness of CFSW are expected to maximize their results, and a minimum wear rate is expected. Hence, the maximum is better principle is used to calculate the signal-to-noise (SN) ratio. For the expectation of a minimum wear rate of weld, the minimum is better principle is considered for the SN ratio calculation[30,35]. The formulae for the SN ratio of maximum and minimum good principles are shown in equations (2) and (3), respectively.

Table 3 Cryogenic friction stir welding parameters and their levels.

FSW Parameters	Levels		
	1 (Low)	**2(Medium)**	**3 (High)**
Tool Pin Profile (TPP)	Cylinder (C)	Stepped cylinder (SC)	Stepped Square (SS)
Rotational speed (RS) (rpm)	800	1000	1200
Welding speed (WS) (mm/min)	80	100	120
Axial Load (AL) (N)	4000	5000	6000

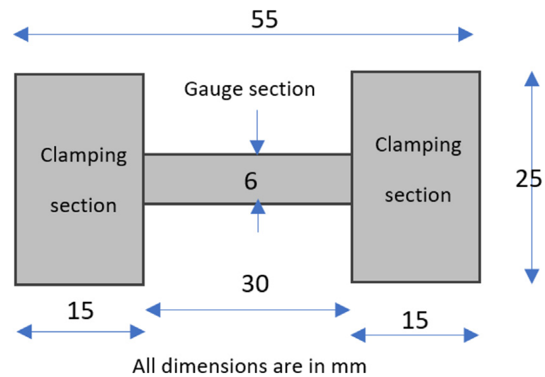

Fig. 3 Schematic arrangement of the ASTM E-2448 specimen for the tensile test.

$$SN\,ratio\,(tensile\ \ strength\ \ and\ \ hardness) = -10\,log\left(\frac{1}{p}\,(\textstyle\sum_{k=1}^{p}\frac{1}{y_k})\right)\ \mathrm{dB}$$

$$SN\,ratio\,(wear\,rate) = 10\,log\left(\frac{1}{p}\,(\textstyle\sum_{k=1}^{p}y_k)\right)\ \mathrm{dB} \quad (3)$$

where "p" is the number of replications of the response variable (y_k) for the "k" number of trials. The SN ratios of the tensile strength, hardness, and wear rate are shown in Table 5. The large S/N values of the welding characteristics are considered optimal settings [27,36].

3. Results and discussion

In this research, the mean values of the responses have been taken to examine the impacts of individual and interaction effects of parameters. The ANOVA (analysis of variance) tests for tensile strength, hardness, and wear rate have been performed in Tables 6, 7, and 8, respectively. Figs. 4(a), 7(a), and 10(a) show the effects of individual parameters on the tensile strength, hardness, and wear rate, respectively. Figs. 4(b), 7 (b), and 10(b) show the effects of interacted parameters on welding characteristics. The confidence interval for all the analyses has been considered to be 0.95 with 5 % of errors. The standard procedure of Taguchi analysis has been followed to obtain the degree of freedom, the sequential sum of the square, adjusted sequential sum of the square, variance, F-value, and percentage of contribution[37].

3.1. Effects of CFSW parameters on tensile strength

The individual and interaction terms of process parameters for tensile strength are considered in Taguchi's analysis (Table 6). Figs. 4(a) and 4(b) depict the effects of individual and interacted parameters on tensile strength, respectively. RS, WS, and AL significantly contributed to improving the tensile strength. The percentages of contributions for TPP, RS, WS, and AL are 30.97 %, 28.31 %, 13.81 %, and 25.99 %, respectively. TPP × RS, TPP × WS, and TPP × AL contributed insignificantly to tensile strength due to their less than 5 % conformance interval [38,39]. The percentages of contributions for terms: TPP × RS, TPP × WS, TPP × AL are 0.19 %, 0.09 %, and 0.17 %, respectively. Thus, all interactive terms

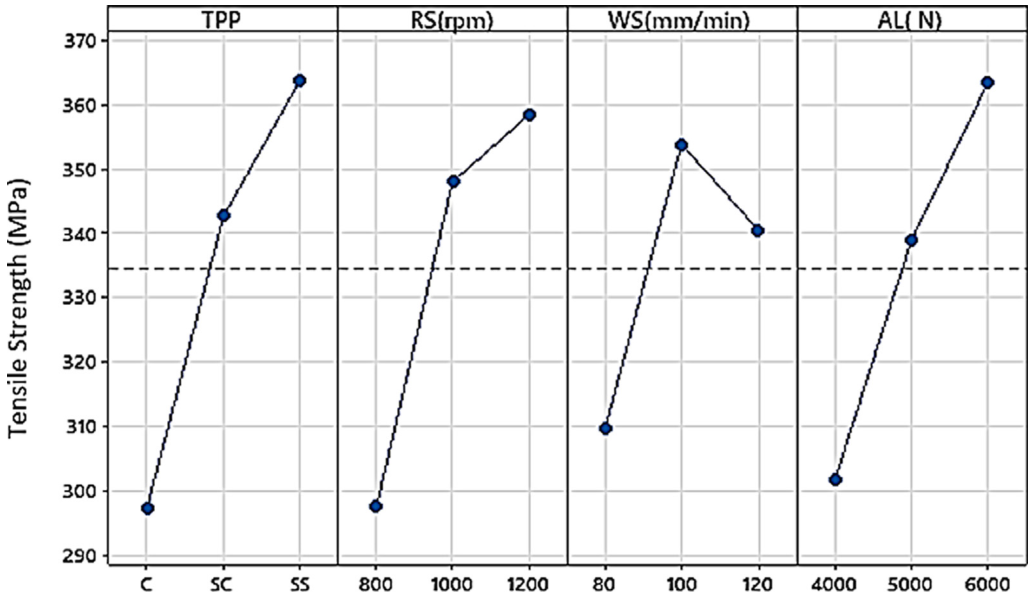

Fig. 4a Effects of individual process parameters on tensile strength.

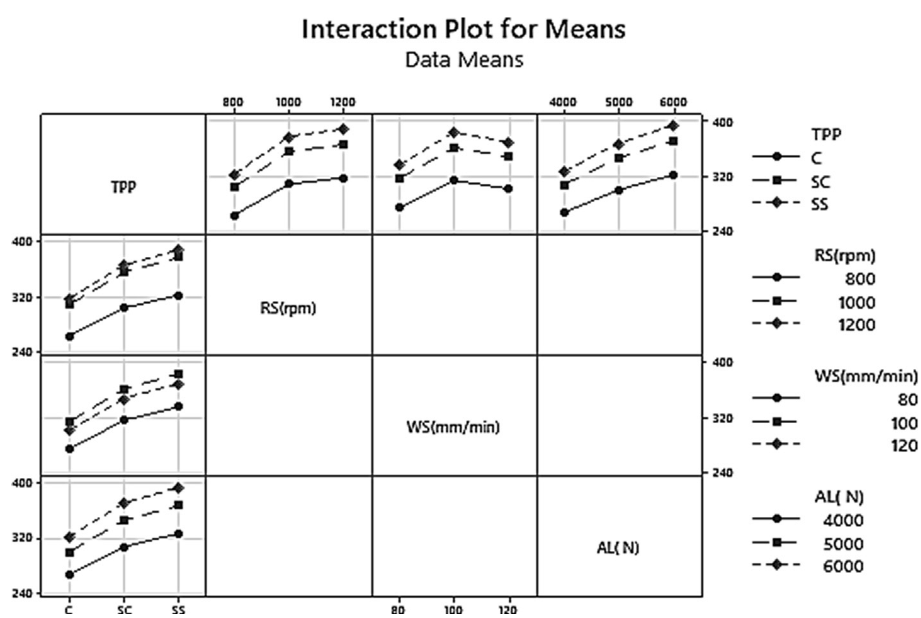

Fig. 4b Interaction Effects of process parameters on Tensile Strength.

are insignificantly connected to maximize the tensile strength due to a less than 5 % confidence interval. Insignificant effects of interaction parameters are also confirmed by the interaction graphs in Fig. 4(b). The residual error has been calculated at 0.46 %. The tensile strength has momentously been improved by increasing rotational speed and axial load due to recrystallization [19,23]. The maximum tensile strength was attained by the stepped square shape of the tool rather than the cylindrical and stepped cylinder shapes due to the increase in stir efficiency (Fig. 4(a)) [40]. It was also enhanced by increasing welding speed up to 100 mm/min and reducing further increasing welding speed due to the non-uniform distribution of grains [23,41]. To attain the maximum tensile strength (442 MPa), 1200 rpm rotational speed, 100 mm/min welding speed, and 6000 N axial load (TPP_3-RS_3-WS_2-AL_3) are recommended.

Fig. 5 illustrates the stress–strain curves for the base ZE42 alloy, normal FSW, and CFSW to analyse the fracture mechanism. Before going for the systematic Taguchi's experiments, the tensile strength and strain of the base ZE42 alloy have been examined. Initially, the percentage of strain was improved by increasing stress or load up to the yield limit (198 MPa). The ultimate tensile strength of the ZE42 base material is 218 MPa with a maximum elongation of 4.5 %. It was also observed that the ductile nature of fracture behaviour was represented. The optimum condition (TPP_3-RS_3-WS_2-AL_3) is used to fabricate the specimen to conduct the tensile tests for both normal FSW and CFSW processes. During the normal

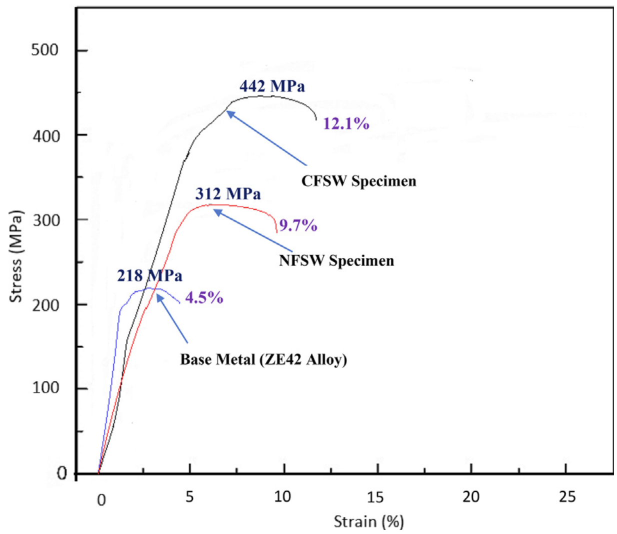

Fig. 5 Stress and Strain curves for base ZE42 alloy, NFSW and CFSW Specimens under optimum condition (TPP: SS; RS: 1200 rpm; WS: 100 mm/min; AL: 6000 N).

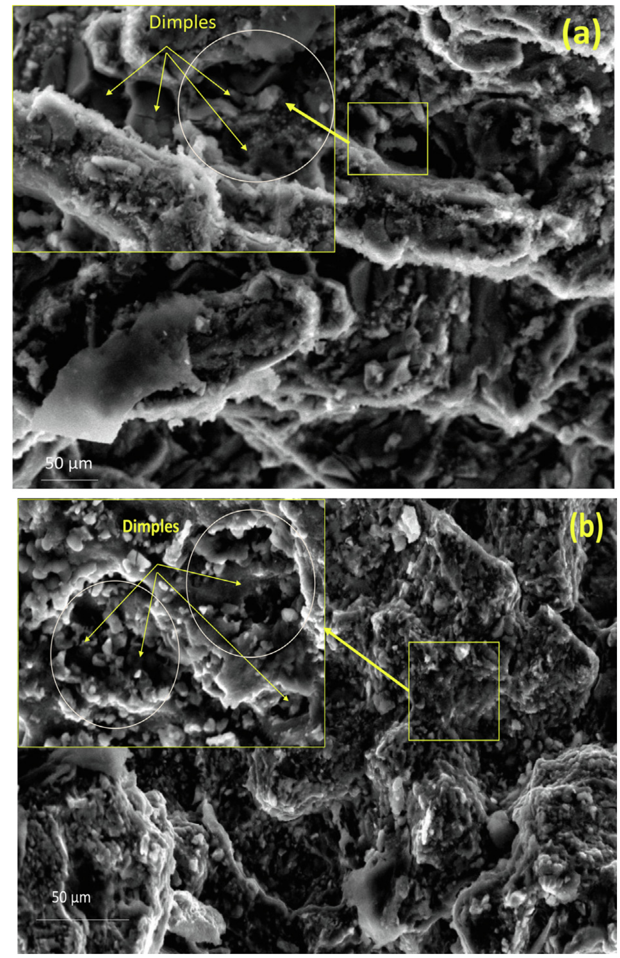

Fig. 6 Comparisons between fractography of tensile tested specimens using optimal settings for (a) CFSW and (b) NFSW.

FSW process, the ductility of the welding joints has improved when compared to the base alloy. The ultimate tensile strengths of the normal FSW and CFW are 312 MPa and 442 MPa, respectively. The percentages of elongation in CFSW and NFSW are 9.7 % and 12.1 %, respectively. Thus, the tensile strength is significantly enhanced by CFSW when compared to the normal FSW process. The ductile fracture of welding joints has been obtained in both the NFSW and CFSW processes due to recrystallization by the stepped square pin tool[19,23,42,43].

Fig. 6(a) and (b) show the fractography of tensile tested specimens of the CFSW and NFSW processes using Taguchi's Optimum setting. The smooth and uniform distribution of grain structure is evident in the CFSW specimen when compared to the NFSW specimen[44]. The collection of dimples or pits is obtained on the tear edges and tensile fractured surfaces of the fractography. It is also confirmed that the ductile fracture occurred in the welded specimen during the tensile test. When compared to the NFSW process, the collection of fine dimples was fashioned on fractured surfaces during the CFSW process. It was observed from strain-strain curves and fractography analysis that the ductile nature fractures occurred in the welding of ZE42 alloy.

3.2. *Effects of cryogenic FSW parameters on hardness*

Fig. 7(a) and Fig. 7(b) illustrate the effects of individual and interaction terms on the hardness of the CFSW process. The ANOVA test for hardness is shown in Table 7. The main parameters: TPP, RS, WS, and AL are significantly involved in enhancing the welding hardness (Fig. 7(a)). The percentages of contributions for TPP, RS, WS, and AL are 37.24 %, 18.49 %, 17.26 %, and 26.16 %, respectively. TPP × RS, TPP × WS, and TPP × AL contributed insignificantly to hardness due to less than 5 % confidence level[38,39]. It was revealed that interaction terms: TPP × RS, TPP × WS, and TPP × AL insignificantly participated in maximizing the hardness of the CFSW joint (Fig. 7(b)). The percentages of contributions for terms: TPP × RS, TPP × WS, TPP × AL are 0.15 %, 0.14 %, and 0.21 % respectively. Thus, all interactive terms are insignificantly connected to maximize the hardness due to a lower than 5 % confidence interval. Insignificant effects of interaction parameters are also confirmed by the interaction graphs in Fig. 7(b). The residual error has been determined to be 0.34 %.

According to Taguchi's analysis, the stepped square-shaped tool pin is strongly recommended to attain maximum hardness. When compared to other tool pin profiles, the square tool pin profile produces metallurgically strong and defect-free joints[42]. The square-shaped pin ensures uniform mixing and distribution of materials on both the retreating and advancing sides due to adequate shearing in the materials. As a result of the uniform distribution in the stir zone, the square tool pin achieves maximum tensile strength and hardness[43]. The stepped square tool in the CFSW process also improved tensile strength, wear resistance, and corrosion resistance in the welding zone [3]. The moderate welding speed, maximum tool rotational speed, and high axial load have been used to obtain the maximum hardness of the welding joint. While increasing rotational speed, hardness is improved by maximum heat in the stir-zone and suddenly cooled by a liquid

Table 4 Experimental observations using L27 Taguchi's design.

Ex. No.	TPP	RS (rpm)	WS (mm/min)	AL (N)	Experimental observations					
					Tensile Strength (MPa)		Hardness (BHN)		Wear rate (mm^3/Nm)	
					Trial 1	Trial 2	Trial 1	Trial 2	Trial 1	Trial 2
1	C	800	80	4000	214.36	220.50	66.7	66.8	2.00	1.97
2	C	800	100	5000	284.55	282.69	88.3	84.4	1.86	1.91
3	C	800	120	6000	289.97	296.11	87.7	87.8	1.85	1.82
4	C	1000	80	5000	292.32	284.46	84.4	82.5	1.84	1.81
5	C	1000	100	6000	356.94	355.08	107.2	105.4	1.67	1.67
6	C	1000	120	4000	282.15	284.29	80.0	84.1	1.84	1.84
7	C	1200	80	6000	322.93	317.07	96.1	92.2	1.68	1.71
8	C	1200	100	4000	300.88	307.02	91.9	90.1	1.76	1.76
9	C	1200	120	5000	332.77	330.91	96.0	92.2	1.79	1.76
10	SC	800	80	4000	249.29	251.43	70.9	73.1	1.86	1.89
11	SC	800	100	5000	323.41	329.55	95.2	91.4	1.79	1.76
12	SC	800	120	6000	339.71	335.85	93.7	95.8	1.75	1.71
13	SC	1000	80	5000	330.37	334.51	92.1	88.2	1.72	1.72
14	SC	1000	100	6000	410.13	410.27	116.7	112.8	1.55	1.60
15	SC	1000	120	4000	329.20	323.34	88.5	88.6	1.72	1.75
16	SC	1200	80	6000	368.24	368.38	102.6	100.7	1.61	1.59
17	SC	1200	100	4000	348.01	352.15	98.2	98.4	1.65	1.67
18	SC	1200	120	5000	382.86	381.00	100.6	102.7	1.66	1.69
19	SS	800	80	4000	263.98	268.12	83.5	81.6	1.62	1.64
20	SS	800	100	5000	348.51	344.65	107.9	106.0	1.54	1.55
21	SS	800	120	6000	360.27	356.41	110.5	106.7	1.50	1.51
22	SS	1000	80	5000	350.83	354.97	105.3	101.5	1.50	1.49
23	SS	1000	100	6000	438.10	432.24	132.6	130.7	1.36	1.37
24	SS	1000	120	4000	346.52	346.66	100.4	102.5	1.51	1.50
25	SS	1200	80	6000	395.11	387.25	115.5	117.7	1.40	1.38
26	SS	1200	100	4000	369.54	373.68	110.6	114.8	1.43	1.46
27	SS	1200	120	5000	407.56	403.70	117.5	115.7	1.44	1.47

nitrogen medium. The hardness is improved by adding pressure to the welding zone while increasing the tool axial load during the CFSW. At the low and high speeds of welding, the material distribution in the stir zone is not uniform. Finally, the average welding speed is associated with attaining the maximum hardness. Thus, a stepped square-shaped tool-tip, 1200 rpm rotational speed, 100 mm/min welding speed, and 6000 N axial load (TPP_3-RS_3-WS_2-AL_3) are predicted to attain the maximum hardness (134.32 BHN) of the CFSW joint of ZE42 alloy.

The variations in hardness between the CFSW and NFSW welding zones are illustrated in Fig. 8. It was observed that the maximum hardness of CFSW and NFSW was attained at 134.32 BHN and 101.6 BHN, respectively. Thus, the hardness of both CFSW and NFSW joints at the stir zone is also higher than the base plate. Welding defects were also observed during the NFSW process due to the instability of the ZE42 alloy at peak temperature[15,45]. It has been experimentally proven that the defect-free welding characteristics of CFSW have been improved by the liquid nitrogen applied in the FSW process. Due to the high peak temperature in the stir zone, the void defect was formed during the NFSW process by melting base metal. Thus, the hardness of the stir zone of NFSW is very low (101.6 BHN) due to the void present in the SZ [28]. The base metal (BM), heat-affected zone (HAZ), thermo-mechanically-affected zone (TMAZ), and stir zone (SZ) in the advanced side and retracting side of the CFSW of the ZE42 alloy are illustrated in Fig. 9. It was observed that grain structure modifications from the BM zone to the SZ are represented. The ductility of welding has been improved by fine grains reformed in the SZ. Thus, the tensile strength, hardness, and wear resistance have been improved by changing the grain structure through the CFSW process.

3.3. Effects of cryogenic FSW parameters on wear rate

The results of Taguchi analysis for minimising the wear rate are illustrated in Table 8. The statistical terms: TPP, RS, WS, AL, and TPP × RS are significantly contributed to minimising the wear rate. The percentages of contributions for TPP, RS, WS, and AL are 72.272 %, 15.321 %, 2.483 %, and 9.728 %, respectively. The stepped square tool pin profile strongly contributes (72.272 %) to wear rate due to uniform material distribution by increasing stir efficiency. The uniform distribution of materials in the stir zone is achieved by the square-shaped pin due to the increasing strength and hardness of the surfaces[43]. While increasing rotational speed, the wear rate is decreased by the uniform reformation of materials in the welding zone. While increasing axial load, the wear rate has also been reduced due to an increase in welding hardness (Fig. 10(a)). The average welding speed is also recommended to minimize the wear rate. The wear rate is increased by an increase in high heat at maximum welding speed. The

Table 5 Percentage of deviation and signal-to-noise ratio.

Ex. No.	Experimental observations: Mean value			Percentage of Error			Signal to noise ratio		
	Tensile Strength (MPa)	Hardness (BHN)	Wear rate (mm3/ Nm)	Tensile Strength	Hardness	Wear rate	Tensile Strength	Hardness	Wear rate
1	217.43	66.7	1.99	2.86	0.21	1.70	46.7438	36.4864	−5.9599
2	283.62	86.4	1.88	0.65	4.37	2.47	49.0546	38.7208	−5.5023
3	293.04	87.8	1.83	2.12	0.16	1.84	49.3371	38.8669	−5.2684
4	288.39	83.4	1.82	2.69	2.20	1.85	49.1972	38.4259	−5.2161
5	356.01	106.3	1.67	0.52	1.73	0.36	51.0292	40.5305	−4.4439
6	283.22	82.0	1.84	0.76	5.18	0.33	49.0423	38.2701	−5.2917
7	320.00	94.2	1.70	1.81	4.02	1.54	50.1019	39.4719	−4.5939
8	303.95	91.0	1.76	2.04	2.02	0.34	49.6547	39.1804	−4.9053
9	331.84	94.1	1.78	0.56	4.02	1.90	50.4185	39.4654	−4.9844
10	250.36	72.0	1.87	0.86	3.02	1.40	47.9711	37.1450	−5.4463
11	326.48	93.3	1.78	1.90	4.05	1.90	50.2760	39.3921	−4.9893
12	337.78	94.7	1.73	1.14	2.28	1.95	50.5723	39.5290	−4.7563
13	332.44	90.1	1.72	1.25	4.19	0.35	50.4338	39.0914	−4.7055
14	410.20	114.8	1.57	0.03	3.31	2.97	52.2599	41.1921	−3.9300
15	326.27	88.5	1.73	1.78	0.16	1.51	50.2705	38.9408	−4.7762
16	368.31	101.6	1.60	0.04	1.81	0.87	51.3243	40.1402	−4.0825
17	350.08	98.3	1.66	1.19	0.14	1.58	50.8829	39.8511	−4.3920
18	381.93	101.6	1.67	0.49	2.13	1.57	51.6396	40.1390	−4.4702
19	266.05	82.6	1.63	1.57	2.23	1.61	48.4985	38.3348	−4.2334
20	346.58	107.0	1.55	1.11	1.72	0.39	50.7957	40.5826	−3.7786
21	358.34	108.6	1.50	1.07	3.49	0.40	51.0855	40.7125	−3.5450
22	352.90	103.4	1.49	1.18	3.67	0.93	50.9526	40.2842	−3.4871
23	435.17	131.7	1.37	1.34	1.40	0.44	52.7726	42.3878	−2.7154
24	346.59	101.5	1.51	0.04	2.13	0.92	50.7963	40.1244	−3.5624
25	391.18	116.6	1.39	1.99	1.85	1.00	51.8462	41.3321	−2.8667
26	371.61	112.7	1.44	1.12	3.74	1.82	51.4013	41.0333	−3.1797
27	405.63	116.6	1.46	0.95	1.58	1.80	52.1623	41.3317	−3.2576

Table 6 Taguchi Analysis for mean values of tensile strength.

Terms	Degree of freedom	Sequential sum of square	Adjusted Sequential sum of square	Variance	F- Value	Percentage of Contribution
TPP	2	20635.9	20635.90	10317.9	200.79	30.97
RS (rpm)	2	18868.0	18868.00	9434.0	183.59	28.31
WS (mm/min)	2	9205.5	9205.50	4602.8	89.57	13.81
AL (N)	2	17320.6	17320.60	8660.3	168.53	25.99
TPP × RS	4	128.5	128.50	32.1	0.62	0.19
TPP × WS	4	60.4	60.40	15.1	0.29	0.09
TPP × AL	4	115.1	115.10	28.8	0.56	0.17
Residual Error	6	308.3	308.30	51.4	–	0.46
Total	26	66642.3	–	–	–	100

TPP × RS, TPP × WS, and TPP × AL contributed insignificantly to the wear rate due to a lower than 5 % confidence interval[38,39]. The percentages of contributions for terms: TPP × RS, TPP × WS, TPP × AL are 0.102 %, 0.017 %, and 0.0 %,5 % respectively. Thus, all interactive terms are insignificant to reduce wear rate. Insignificant effects of interaction parameters on the wear rate are also established in the interaction graphs of Fig. 10(b). The residual error has been obtained at 0.011 %. Thus, a stepped-square tool tip with maximum rotational speed (1200 rpm), with a mean welding speed of 100 mm/min, and a maximum axial load of 6000 N (TPP_3-RS_3-WS_2-AL_3) is predicted to minimize the wear rate (1.3 mm^3/Nm) of the CFSW joint.

The sliding direction and delaminated debris locations on the welded surfaces of both NFSW and CFSW specimens are illustrated in Fig. 11(a) and Fig. 11(b), respectively. The worn-out spots on the CFSW are finer than NFSW specimens. The material strength has been improved by fine grain formation due to the reduction of peak temperature and plastic state of material flow during the CFSW process[18]. The softening and plasticizing of the ZE42 alloy material occurred by increasing the frictional heat between the tool and the work materials during the NFSW process[3]. Thus, wear delamina-

Table 7 Taguchi Analysis for Mean values of hardness.

Terms	Degree of freedom	Sequential sum of square	Adjusted Sequential sum of square	Variance	F- Value	Percentage of Contribution
TPP	2	2047.38	2047.38	1023.69	328.34	37.24
RS (rpm)	2	1016.79	1016.79	508.40	163.06	18.49
WS (mm/min)	2	948.91	948.91	474.45	152.18	17.26
AL (N)	2	1438.45	1438.45	719.22	230.68	26.16
TPP × RS	4	8.46	8.46	2.11	0.68	0.15
TPP × WS	4	7.59	7.59	1.90	0.61	0.14
TPP × AL	4	11.74	11.74	2.93	0.94	0.21
Residual Error	6	18.71	18.71	3.12	–	0.34
Total	26	5498.02	–	–	–	100

Table 8 Taguchi Analysis for mean values of wear rate.

Terms	Degree of freedom	Sequential sum of square	Adjusted Sequential sum of square	Variance	F- Value	Percentage of Contribution
TPP	2	0.49908	0.49908	0.24954	19029.27	72.272
RS (rpm)	2	0.10580	0.10580	0.05290	4034.03	15.321
WS (mm/min)	2	0.01715	0.01715	0.00857	653.74	2.483
AL (N)	2	0.06718	0.06718	0.03359	2561.49	9.728
TPP*RS	4	0.00071	0.00071	0.00018	13.46	0.102
TPP*WS	4	0.00011	0.00011	0.00003	2.18	0.017
TPP*AL	4	0.00045	0.00045	0.00011	8.55	0.065
Residual Error	6	0.00008	0.00008	0.00001	–	0.011
Total	26	0.69055	–	–	–	100

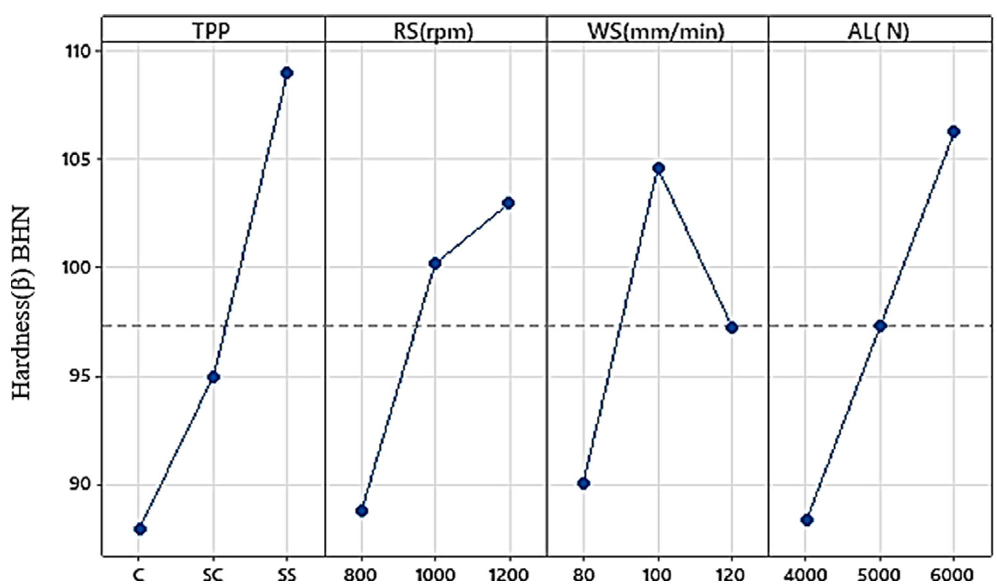

Fig. 7a Effects of individual process parameters on hardness.

tion and debris rates are higher in the NFSW process due to the lower hardness and strength of the welded surface (Fig. 11(a)). This delamination mechanism has the potential to increase the wear rate of NFSW specimens. The delamination and surface debris have been significantly reduced under the cryogenic (liquid nitrogen) temperature by improving the material battle to crack nucleation and propagation (Fig. 11 (b)) [3,21]. Thus, the wear rate of the CFSW (1.3 mm^3/Nm) is lower than the NFSW process (1.7 mm^3/Nm).

3.4. Confirmation experiments for Taguchi analysis

The significant parameter levels are predicted by Taguchi analysis and validated by conducting conformation experiments. The interaction terms were not included to perform these experiments. The percentage of deviation of predicted responses with confirmation experimental values is shown in Table 9. It was observed that the percentages of deviation of tensile strength, hardness, and wear rate are 0.167 %,

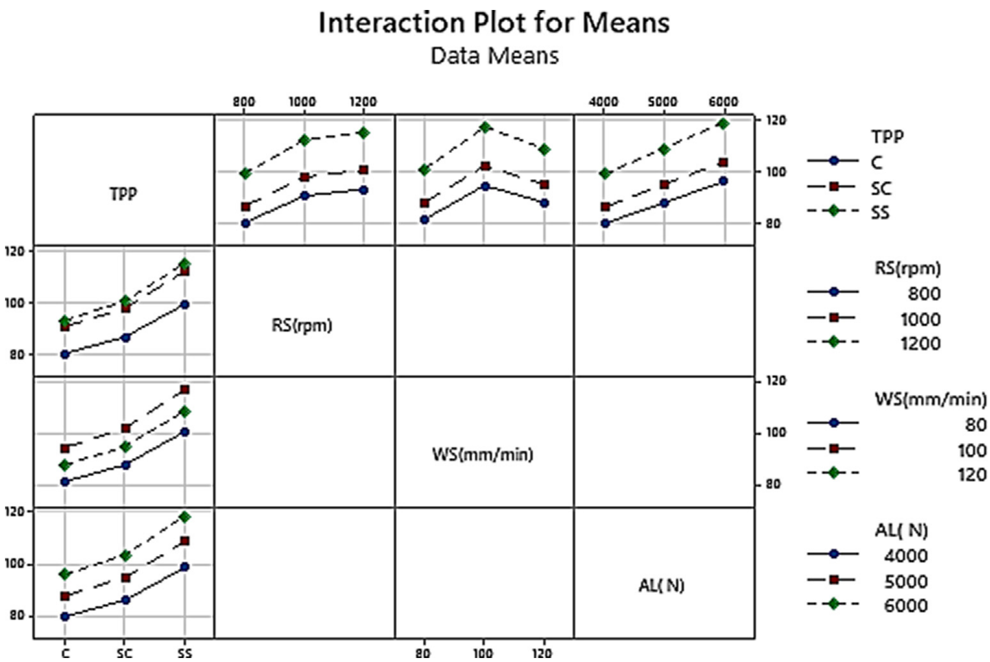

Fig. 7b Interaction Effects of process parameters on hardness.

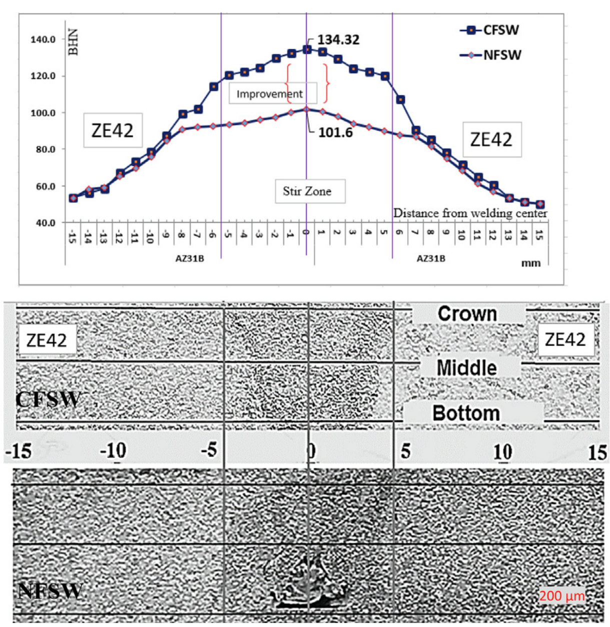

Fig. 8 Comparisons of Hardness of CFSW and NFSW using optimum setting (TPP$_3$-RS$_3$-WS$_3$-AL$_3$).

0.652 %, and 2.86 % respectively which are less than 5 % of the confidence level [33,34]. Thus, a stepped square tool tip, 1200 rpm of tool rotation, 100 mm/min welding speed, and 6000 N axial trust are recommended to obtain the optimum solutions for all responses. These predicted parameter settings have been used to compare the CFSW and NFSW performances.

3.5. Comparisons between CFSW and NFSW processes

The comparison of the welding performances of NFSW and CFSW is illustrated in Fig. 12. It was revealed that the tensile strength, hardness, and wear resistance of CFSW processes are significantly improved when compared to NFSW processes. It was revealed that the hardness of CFSW is 35.13 % higher than NFSW. The 41.36 % tensile strength of the CFSW process is higher than the NFSW process. The wear rate of CFSW is 23.53 %, lower than NFSW. In the CFSW of ZE42 alloys, high heat generation in the stir zone has been minimized by applying liquid nitrogen in the welding zone. The uniform grain structure and recrystallization are enhanced during the CFSW process.

4. Conclusions

The CFSW of similar ZE42 alloy plates has been performed to improve the welding characteristics using Taguchi's technique. The microstructure of CFSW characteristics is examined using SEM images. While increasing rotation speed and axial load, tensile strength and hardness are improved, and the wear rate of the CFSW process is reduced. The stepped square tool tip is used to improve the welding characteristics when compared to other profiles. The average welding speed is recommended to improve all welding properties. The following welding parameters: stepped square tool with RS$_3$: 1200 rpm, WS$_2$: 100 mm/min, and AL$_3$: 6000 N are estimated to attain the best welding characteristics (Tensile Strength: 442 MPa; Hardness: 134.32 BHN; Wear Rate: 1.3 mm^3/Nm). Microstructure, and fractography analysis have been performed to compare the welding characteristics of CFSW and NFSW processes. A defect-free welding joint has been achieved by the CFSW process when compared to NFSW. The worn-out surface of the CFSW specimen has fewer abrasions than the NFSW specimen. It was

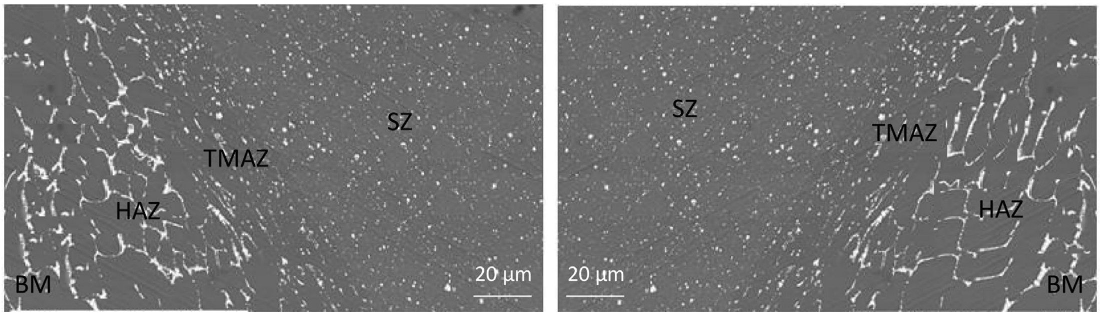

Fig. 9 Various zones in the Advanced side and retracting side of CFSW of ZE42 alloy.

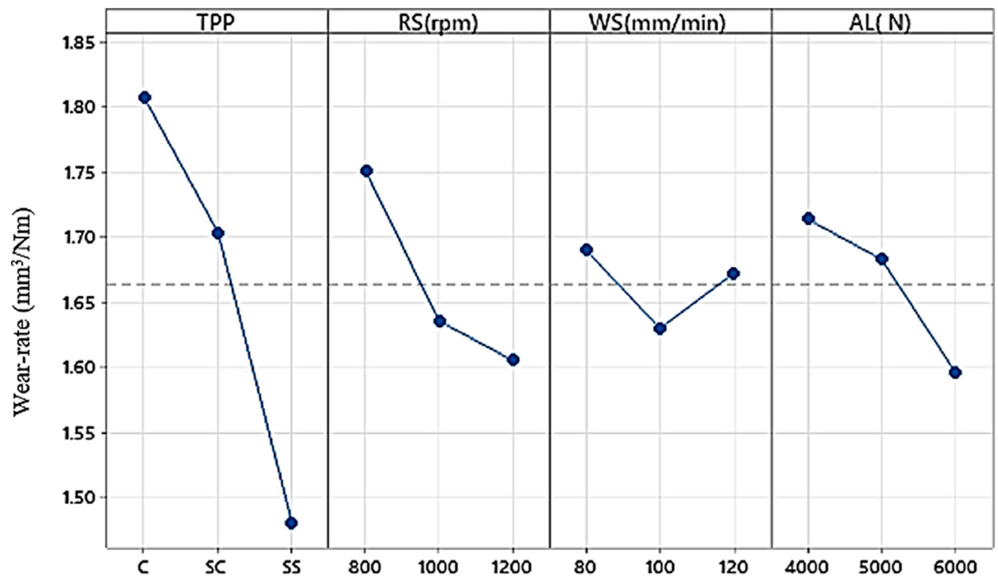

Fig. 10a Effects of individual process parameters on wear rate.

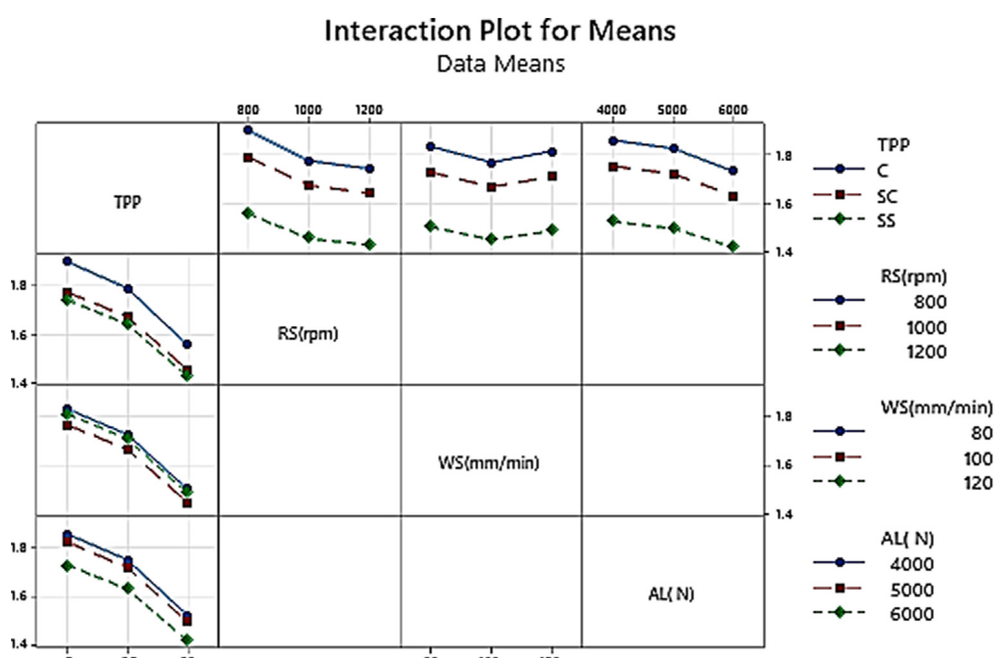

Fig. 10b Interaction Effects of process parameters on wear rate.

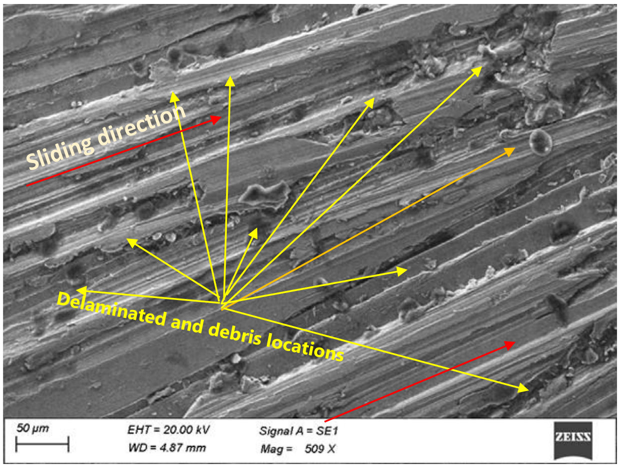

Fig. 11a Worn-out surface NFSW (wear rate: 1.7 mm^3/Nm).

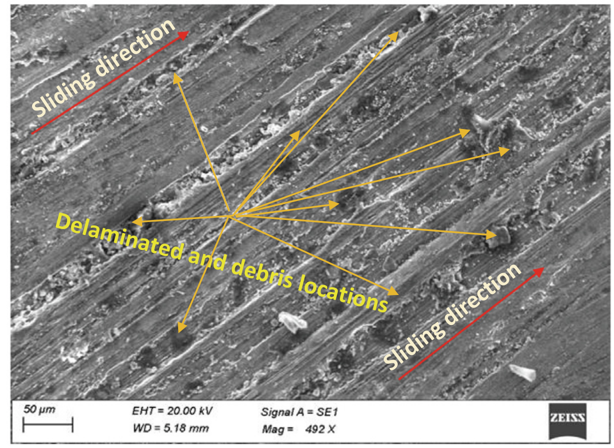

Fig. 11b Worn-out surface CFSW (wear rate: 1.3 mm^3/Nm).

Table 9 Validation for Taguchi predicted results using confirmation experiment.

S. No.	Process parameter				Response value		Percentage of deviation	Welding Characteristics
	TPP	RS (rpm)	WS (mm/min)	AL (N)	Predicted Result	Experiments		
1	SS	1200	100	6000	441.26	442.00	0.167 %	Tensile Strength (MPa)
2	SS	1200	100	6000	133.45	134.32	0.652 %	Hardness (BHN)
3	SS	1200	100	6000	1.33828	1.30	2.860 %	Wear rate (mm^3/Nm)

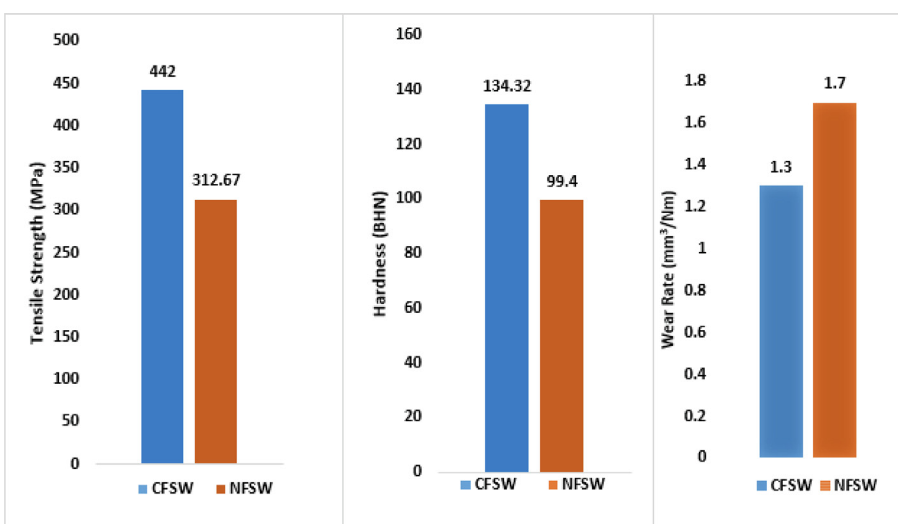

Fig. 12 Comparisons of the welding characteristics of CFSW and NFSW processes.

concluded that the tensile strength and hardness of CFSW were improved by 41.36 % and 35.13 %, respectively, and the wear rate had decreased by 23.53 % when compared to NFSW process.

Declaration of Competing Interest

The authors declare that they have no known competing financial interests or personal relationships that could have appeared to influence the work reported in this paper.

Acknowledgement

This work was supported by the Project of Excellence, Faculty of Science, University of Hradec Králové, No. 2210/2023-2024.

References

[1] W.C. Ke, J.P. Oliveira, S.S. Ao, F.B. Teshome, L. Chen, B. Peng, Z. Zeng, Thermal process and material flow during dissimilar double-sided friction stir spot welding of AZ31/ZK60 magnesium alloys, J. Mater. Res. Technol. 17 (2022) 1942–1954, https://doi.org/10.1016/j.jmrt.2022.01.097.

[2] W. Xu, H. Li, J. Yang, Y. Zhao, J.P. Oliveira, H. Liu, Z. Zhang, C. Tan, Dynamic wetting and spreading mechanisms regulated by elemental Ni in a Mg/steel immiscible system during laser processing, J. Manuf. Process. 80 (2022) 600–611, https://doi.org/10.1016/j.jmapro.2022.06.042.

[3] C. Rathinasuriyan, R. Sankar, Wear and Corrosion Behavior of Cryogenic Friction Stir Processed AZ31B Alloy, J. Mater. Eng. Perform. 30 (2021) 3118–3128, https://doi.org/10.1007/s11665-021-05636-0.

[4] P. Cavaliere, P.P. De Marco, Effect of friction stir processing on mechanical and microstructural properties of AM60B Magnesium alloy, J. Mater. Sci. 41 (2006) 3459–3464, https://doi.org/10.1007/s10853-005-5601-9.

[5] F.R. Chiuzuli, B.F. Batistão, L.A. Bergmann, N.G. de Alcântara, J.F. dos Santos, B. Klusemann, P. Gargarella, Effect of the gap width in AZ31 magnesium alloy joints obtained by friction stir welding, J. Mater. Res. Technol. 15 (2021) 5297–5306, https://doi.org/10.1016/j.jmrt.2021.10.115.

[6] K. Hono, C.L. Mendis, T.T. Sasaki, K. Oh-Ishi, Towards the development of heat-treatable high-strength wrought Mg alloys, Scr. Mater. 63 (2010) 710–715, https://doi.org/10.1016/j.scriptamat.2010.01.038.

[7] W. Xunhong, W. Kuaishe, Microstructure and properties of friction stir butt-welded AZ31 magnesium alloy, Mater. Sci. Eng. A. 431 (2006) 114–117, https://doi.org/10.1016/j.msea.2006.05.128.

[8] F. Chai, D. Zhang, Y. Li, Effect of thermal history on microstructures and mechanical properties of AZ31 magnesium alloy prepared by friction stir processing, Materials (Basel). 7 (2014) 1573–1589, https://doi.org/10.3390/ma7031573.

[9] F. Chai, D. Zhang, Y. Li, Microstructures and tensile properties of submerged friction stir processed AZ91 magnesium alloy, J. Magnes. Alloy. 3 (2015) 203–209, https://doi.org/10.1016/j.jma.2015.08.001.

[10] G. Cao, D. Zhang, F. Chai, W. Zhang, C. Qiu, Superplastic behavior and microstructure evolution of a fine-grained Mg-Y-Nd alloy processed by submerged friction stir processing, Mater. Sci. Eng. A. 642 (2015) 157–166, https://doi.org/10.1016/j.msea.2015.06.086.

[11] X. Feng, H. Liu, J.C. Lippold, Microstructure characterization of the stir zone of submerged friction stir processed aluminum alloy 2219, Mater. Charact. 82 (2013) 97–102, https://doi.org/10.1016/j.matchar.2013.05.010.

[12] F. Rui-dong, S. Zeng-qiang, S. Rui-cheng, L. Ying, L. Hui-jie, L. Lei, Improvement of weld temperature distribution and mechanical properties of 7050 aluminum alloy butt joints by submerged friction stir welding, Mater. Des. 32 (2011) 4825–4831, https://doi.org/10.1016/j.matdes.2011.06.021.

[13] Q. Wang, Z. Zhao, Y. Zhao, K. Yan, H. Zhang, The adjustment strategy of welding parameters for spray formed 7055 aluminum alloy underwater friction stir welding joint, Mater. Des. 88 (2015) 1366–1376, https://doi.org/10.1016/j.matdes.2015.09.038.

[14] N. Bhadouria, L. Thakur, P. Kumar, N. Arora, An investigation of normal and submerged condition on microstructural and tribological properties of friction stir processed AZ91-D magnesium alloy, Can. Metall. Q. 56 (2017) 94–103, https://doi.org/10.1080/00084433.2016.1270394.

[15] M.A. Mofid, A. Abdollah-zadeh, F. Malek Ghaini, The effect of water cooling during dissimilar friction stir welding of Al alloy to Mg alloy, Mater. Des. 36 (2012) 161–167, https://doi.org/10.1016/j.matdes.2011.11.004.

[16] Y. Wang, R. Fu, Y. Li, L. Zhao, A high strength and high electrical conductivity Cu-Cr-Zr alloy fabricated by cryogenic friction stir processing and subsequent annealing treatment, Mater. Sci. Eng. A. 755 (2019) 166–169, https://doi.org/10.1016/j.msea.2019.04.004.

[17] A. Bansal, A.K. Singla, V. Dwivedi, D.K. Goyal, J. Singla, M. K. Gupta, G.M. Krolczyk, Influence of cryogenic treatment on mechanical performance of friction stir Al-Zn-Cu alloy weldments, J. Manuf. Process. 56 (2020) 43–53, https://doi.org/10.1016/j.jmapro.2020.04.067.

[18] S. Park, H. Nam, J. Park, Y. Na, H. Kim, N. Kang, Superior-tensile property of CoCrFeMnNi alloys achieved using friction-stir welding for cryogenic applications, Mater. Sci. Eng. A. 788 (2020), https://doi.org/10.1016/j.msea.2020.139547 139547.

[19] M.V.N.V. Satyanarayana, A. Kumar, Microstructure Evolution, Mechanical, and Corrosion Behavior of Cryogenic Friction Stir-Processed AA2014 Alloy, Adv. Eng. Mater. 23 (2021), https://doi.org/10.1002/adem.202100301.

[20] F. Khodabakhshi, A.P. Gerlich, A. Simchi, A.H. Kokabi, Cryogenic friction-stir processing of ultrafine-grained Al-Mg-TiO2 nanocomposites, Mater. Sci. Eng. A. 620 (2015) 471–482, https://doi.org/10.1016/j.msea.2014.10.048.

[21] H.S. Arora, H. Singh, B.K. Dhindaw, Wear behaviour of a Mg alloy subjected to friction stir processing, Wear. 303 (2013) 65–77, https://doi.org/10.1016/j.wear.2013.02.023.

[22] A.K. Darwins, M. Satheesh, G. Ramanan, Alloys Aa7075 and Mg Ze42 Using Butt Joint, Geometry 8 (2018) 505–512.

[23] Y. Zhao, Z. Lu, K. Yan, L. Huang, Microstructural characterizations and mechanical properties in underwater friction stir welding of aluminum and magnesium dissimilar alloys, Mater. Des. 65 (2015) 675–681, https://doi.org/10.1016/j.matdes.2014.09.046.

[24] S. Boopathi, K. Sivakumar, Study of water assisted dry wire-cut electrical discharge machining, Indian J. Eng. Mater. Sci. 21 (2014) 75–82. https://doi.org/http://nopr.niscair.res.in/handle/123456789/27453.

[25] V. Haribalaji, S. Boopathi, M. Mohammed Asif, T. Yuvaraj, D. Velmurugan, K. Anton Savio Lewise, S. Sudhagar, P. Suresh, Influences of Mg-Cr filler materials in Friction Stir Process of Aluminium-based dissimilar alloys, Mater. Today Proc. 66 (2022) 948–954. https://doi.org/10.1016/j.matpr.2022.04.668.

[26] V.S. Jatti, Multi-characteristics optimization in EDM of NiTi alloy, NiCu alloy and BeCu alloy using Taguchi's approach and utility concept, Alexandria Eng. J. 57 (2018) 2807–2817, https://doi.org/10.1016/j.aej.2017.11.004.

[27] S. Boopathi, Performance Improvement of Eco-Friendly Near-Dry Wire-Cut Electrical Discharge Machining Process Using Coconut Oil-Mist Dielectric Fluid, J. Adv. Manuf. Syst. (2023), https://doi.org/10.1142/S0219686723500178.

[28] A. Ampaiboon, O.U. Lasunon, B. Bubphachot, Optimization and Prediction of Ultimate Tensile Strength in Metal Active Gas Welding, Sci. World J. 2015 (2015) 1–5, https://doi.org/10.1155/2015/831912.

[29] S.K. Naimuddin, M.T. Ahamad, B.P.C. Sekhar, P.N. Mohan, V. Kampurath, Y. Ali, Wear behaviour of welded and non-welded samples of friction stir welding of similar and dissimilar joints of aluminium alloys (AA6061-AA6061), (AA6082-AA6082) & (AA6061-AA6082) under T6 condition, Int. J. Mech. Eng. Technol. 7 (2016) 289–299.

[30] V. Haribalaji, S. Boopathi, M.M. Asif, Optimization of friction stir welding process to join dissimilar AA2014 and AA7075 aluminum alloys, Mater. Today Proc. 50 (2021) 2227–2234, https://doi.org/10.1016/j.matpr.2021.09.499.

[31] S. Boopathi, V. Haribalaji, M. Mageswari, M.M. Asif, Influences of Boron Carbide Particles on the Wear Rate and Tensile Strength of Aa2014 Surface Composite Fabricated By Friction-Stir Processing, Mater. Tehnol. 56 (2022) 263–270. https://doi.org/10.17222/mit.2022.409.

[32] S. Boopathi, A. Thillaivanan, M. Pandian, R. Subbiah, P. Shanmugam, Friction stir processing of boron carbide reinforced aluminium surface (Al-B4C) composite: Mechanical characteristics analysis, Mater. Today Proc. 50 (2021) 2430–2435, https://doi.org/10.1016/j.matpr.2021.10.261.

[33] S. Boopathi, K. Sivakumar, Experimental investigation and parameter optimization of near-dry wire-cut electrical discharge machining using multi-objective evolutionary algorithm, Int. J. Adv. Manuf. Technol. 67 (2013) 2639–2655, https://doi.org/10.1007/s00170-012-4680-4.

[34] V. Haribalaji, S. Boopathi, M.M. Asif, M. Jeyakumar, R. Subbiah, K.A.S. Lewise, Influences of Friction stir tool parameters for joining two similar AZ61A alloy plates, Mater. Today Proc. 50 (2021) 2547–2553, https://doi.org/10.1016/j.matpr.2021.12.074.

[35] C. Kavitha, P.S. Geetha Malini, V. Charan Kantumuchu, N. Manoj Kumar, A. Verma, S. Boopathi, An experimental study on the hardness and wear rate of carbonitride coated stainless steel, Mater. Today Proc. (2022). https://doi.org/10.1016/j.matpr.2022.09.524.

[36] S. Boopathi, Cryogenically treated and untreated stainless steel grade 317 in sustainable wire electrical discharge machining process: a comparative study, Environ. Sci. Pollut. Res. 1–10 (2022).

[37] S. Boopathi, An investigation on gas emission concentration and relative emission rate of the near-dry wire-cut electrical discharge machining process, Environ. Sci. Pollut. Res. (2021) 1–10, https://doi.org/10.1007/s11356-021-17658-1.

[38] E. Kannan, Y. Trabelsi, S. Boopathi, S. Alagesan, Influences of cryogenically treated work material on near-dry wire-cut electrical discharge machining process, Surf. Topogr. Metrol. Prop. 10 (2022), https://doi.org/10.1088/2051-672X/ac53e1.

[39] B. Sampath, S. Myilsamy, Experimental investigation of a cryogenically cooled oxygen-mist near-dry wire-cut electrical discharge machining process, Stroj. Vestnik/Journal, Mech. Eng. 67 (2021) 322–330, https://doi.org/10.5545/sv-jme.2021.7161.

[40] D. Zhemchuzhnikova, S. Malopheyev, S. Mironov, R. Kaibyshev, Cryogenic properties of Al-Mg-Sc-Zr friction-stir welds, Mater. Sci. Eng. A. 598 (2014) 387–395, https://doi.org/10.1016/j.msea.2014.01.060.

[41] M.S. Khorrami, M. Kazeminezhad, Y. Miyashita, N. Saito, A. H. Kokabi, Influence of ambient and cryogenic temperature on friction stir processing of severely deformed aluminum with SiC nanoparticles, J. Alloys Compd. 718 (2017) 361–372, https://doi.org/10.1016/j.jallcom.2017.05.234.

[42] K.K. Jangra, N. Sharma, R. Khanna, D. Matta, An experimental investigation and optimization of friction stir welding process for AA6082 T6 (cryogenic treated and untreated) using an integrated approach of Taguchi, grey relational analysis and entropy method, Proc. Inst. Mech. Eng. Part L J. Mater. Des. Appl. 230 (2016) 454–469, https://doi.org/10.1177/1464420715578182.

[43] Y. Kunnathur, P. Ashoka, V. Perumal, Influence of Tool Shoulder Concave Angle and Pin Profile on Mechanical Properties and Microstructural Behaviour of Friction Stir Welded AA7075-T651 and AA6061 Dissimilar Joint, Trans. Indian Inst. Met. (2019), https://doi.org/10.1007/s12666-019-01584-5.

[44] B.K. Gu, D.T. Zhang, Microstructure and cryogenic mechanical properties of AA5083 joints prepared by friction stir welding, Mater. Sci. Forum. 788 (2014) 243–248, https://doi.org/10.4028/www.scientific.net/MSF.788.243.

[45] B. Darras, E. Kishta, Submerged friction stir processing of AZ31 Magnesium alloy, Mater. Des. 47 (2013) 133–137, https://doi.org/10.1016/j.matdes.2012.12.026.